J. Fluid Mech. (2014), vol. 745, pp. 564–591. © Cambridge University Press 2014
doi:10.1017/jfm.2014.91

Extreme solitary waves on falling liquid films

S. Chakraborty[1], **P.-K. Nguyen**[2], **C. Ruyer-Quil**[1,3,‡] **and V. Bontozoglou**[2,†]

[1]Université Pierre et Marie Curie, CNRS, Laboratoire FAST, Campus Universitaire, 91405 Orsay, France
[2]University of Thessaly, Department of Mechanical Engineering, 38334 Volos, Greece
[3]Institut Universitaire de France

(Received 3 September 2013; revised 16 December 2013; accepted 11 February 2014;
first published online 24 March 2014)

Direct numerical simulation (DNS) of liquid film flow is used to compute fully developed solitary waves and to compare their characteristics with the predictions of low-dimensional models. Emphasis is placed on the regime of high inertia, where available models provide widely differing results. It is found that the parametric dependence of wave properties on inertia is highly non-trivial, and is satisfactorily approximated only by the four-equation model of Ruyer-Quil & Manneville (*Eur. Phys. J.* B, vol. 15, 2000, pp. 357–369). Detailed comparison of the asymptotic shapes of upstream and downstream tails is performed, and inherent limitations of all long-wave models are revealed. Local flow reversal in front of the main hump, which has been previously discussed in the literature, is shown to occur for an inertia range bounded from below and from above, and the boundaries are interpreted in terms of the capillary origin of the phenomenon. Computational results are reported for the entire range of Froude numbers, providing benchmark data for all wall inclinations.

Key words: interfacial flows (free surface), capillary flows, low-Reynolds-number flows

1. Introduction

Intensification of heat and mass exchange between a gas and a liquid phase is a key goal in chemical engineering. A common practice is to reduce the thickness of the liquid layer in order to lower its resistance to transfer and to enhance the contact area between the two phases. Liquid film flows are thus widely encountered in industrial processes, for instance in evaporators and multiphase chemical reactors. Falling liquid films over a vertical or inclined plane still constitute the state-of-the-art technical solution whenever pressure drop must be minimized in the gas phase, for instance in vacuum operations, and also when phase change or absorption processes are involved.

For such flows, the presence of wavy dynamics organized into localized structures, or solitary waves, is well known to drastically enhance the exchange rates (Miyara 2000*a*). Yet the exact mechanisms which promote such an enhancement, as well as the optimal flow conditions from the point of view of heat/mass transfer, are

---

† Email address for correspondence: bont@mie.uth.gr

‡ Present address: Université de Savoie, CNRS, Laboratoire LOCIE, Savoie Technolac, 73376 Le Bourget du Lac, France

still matters of current investigation. Recirculation regions, or rolls, at the humps of solitary waves certainly play a role as suggested by Miyara (2000*a*). The transport of liquid by the waves, which participate to the thinning of the film, is another contribution to transfer intensification (Jayanti & Hewitt 1996). It was also predicted computationally (Malamataris, Vlachogiannis & Bontozoglou 2002; Kunugi & Kino 2005; Dietze, Leefken & Kneer 2008; Dietze, AL-Sibai & Kneer 2009) and confirmed experimentally (Tihon *et al.* 2006; Dietze *et al.* 2008, 2009) that solitary waves may promote flow separation and formation of a backflow region near the wall. This phenomenon was shown recently to enhance mass transfer between the film and the wall in the case of a porous substrate (Samanta, Goyeau & Ruyer-Quil 2013).

An accurate description of the structure of solitary waves and of their interactions is thus a prerequisite for systematic progress in the optimization of processes involving falling film flows. The derivation of simplified sets of equations (models), which adequately capture the physical mechanisms involved, occupies a central position in that context for at least two reasons. First, it provides a framework for defining the different flow regimes, identifying the relevant physical effects and applying analytical tools and predictions. Second, it enables a full-scale numerical investigation at a reasonable computational cost.

Along these lines, several improvements have been achieved over the last few decades. Benney (1966) took advantage of the long-wave nature of the primary instability and introduced a film parameter $\epsilon \sim \partial_{x,t}$ accounting for the slow evolution in time and space of the waves when compared to the relatively quick viscous diffusion across the film layer. He then performed an expansion of the flow variables with respect to ϵ and showed that the dynamics of the film is at lowest order enslaved to its kinematics, which is expressed by surface equations or evolution equations for the film thickness h.

Based on Benney's long-wave theory, Pumir, Manneville & Pomeau (1983) described solitary waves in terms of homoclinic orbits in a three-dimensional phase space using dynamical systems theory. They also found spurious finite-time blow-ups of the solutions to the so-called Benney equation, which severely restricts its use to the vicinity of the instability threshold in the parameter space (Scheid *et al.* 2005). This drawback was later overcome by Ooshida (1999) who applied a Padé-like regularization procedure and derived a modified Benney equation. Based on his one-equation model and the computation of the wave characteristics – speed, amplitude and shape – Ooshida identified two different regimes, namely the drag–gravity regime close to the instability onset and the drag–inertia regime where inertia effects become dominant. In the latter case solitary waves are often referred to as capillary roll waves (Balmforth & Liu 2004).

It is now well accepted that the large-amplitude solitary waves reported in the experiments, by e.g. Alekseenko, Nakoryakov & Pokusaev (1985), Liu & Gollub (1994), Leontidis *et al.* (2010) to name but a few, cannot be accurately captured by one-equation models. The reason of this failure is the assumed strict slaving of the velocity field to the evolution of the film thickness h. In order to relax this assumption, one has to introduce extra degrees of freedom (for instance the local flow rate q) and deal with systems of several coupled evolution equations. In an attempt along these lines, Kapitza & Kapitza (1949) and later (Shkadov 1967) formulated a two-equation model by uniformly averaging the continuity and momentum equations as suggested by the classical Kármán–Polhausen approach in boundary-layer theory. Based on this model, Bunov, Demekhin & Shkadov (1986) calculated for the first time a spectrum of solitary waves. However, the Kapitza–Shkadov model lacks consistency with the long-wave expansion and thus introduces a significant error in the prediction of the instability threshold, which severely restricts its interest to the vertical orientation.

Many studies have been undertaken the last two decades along the lines of Shkadov's integral boundary layer (IBL) approach, using different numbers of degrees of freedom and different approximations, such as the centre manifold analysis and a Galerkin weighted-residual technique. As a result, a number of low-dimensional models are now available in the literature (see for instance Yu *et al.* 1995; Roberts 1996; Ruyer-Quil & Manneville 1998, 2000, 2002; Nguyen & Balakotaiah 2000; Panga & Balakotaiah 2003; Roberts & Li 2006 and the reviews by Craster & Matar 2009; Kalliadasis *et al.* 2012). A crucial test for all these models is the correct prediction of the properties of solitary waves, in particular the wave shape, height and phase speed. However, it turns out (Ruyer-Quil & Manneville 2005; Scheid, Ruyer-Quil & Manneville 2006) that, though most of the models predict similar behaviour close to the instability threshold (described by the critical value of the Reynolds number, Re_c), they exhibit large differences from each other for $Re \gg Re_c$, i.e. when inertia becomes significant. This discrepancy severely reduces confidence in their applicability, particularly at high Re.

One means of assessing the performance of low-dimensional models is to compare them to the results of direct numerical simulation (DNS) of the full Navier–Stokes equations and associated wall and free-surface boundary conditions. Over the years, DNS studies have proven an indispensable complementary tool for the understanding of the dynamics of liquid film flow (see for example Bach & Villadsen 1984; Ho & Patera 1990; Salamon, Armstrong & Brown 1994; Ramaswamy, Chippada & Joo 1996; Miyara 2000*b*; Malamataris *et al.* 2002; Gao, Morley & Dhir 2003; Nosoko & Miyara 2004; Kunugi & Kino 2005; Tihon *et al.* 2006; Dietze *et al.* 2008; Trifonov 2012 among others).

However, it appears that none of the above works addressed sufficiently the question of extreme solitary waves, i.e. large waves occurring at high Re and belonging deep in the drag–inertia regime. Thus, the goal of the present work is to use DNS in order to study the characteristics of solitary waves, and in particular their parametric variation with flow inertia. The computed characteristics (wave height, phase speed and shape) will be compared to the predictions of currently available low-dimensional models, and the most accurate among them will be singled out. At the same time, these DNS results will form a benchmark for future modelling efforts.

In what follows, we will consider only single-hump solitary-wave solutions, which are the ones that are actually observed in experiments (e.g. Tihon *et al.* 2006). Multi-hump wave solutions to the Navier–Stokes equations have been discussed in the theoretical literature (e.g. Chang & Demekhin 2002; Trifonov 2012). The paper is organized as follows. The problem is formulated in § 2. In § 3, the understanding gained by low-dimensional models in the framework of dynamical systems theory is recalled. The computational methodology is outlined in § 4 and the results are presented and discussed in § 5. Finally, the main conclusions are summarized in § 6.

2. Problem formulation

This study deals with liquid films flowing under the action of gravity g along a plane inclined at an angle β with the horizontal, as sketched in figure 1. The flow is free of shear force at the gas–liquid interface. The problem is modelled as two-dimensional in a Cartesian coordinate system, with the x-axis pointing in the mean flow direction and the y-axis across the film. The velocity field is denoted by $\boldsymbol{u}$ with

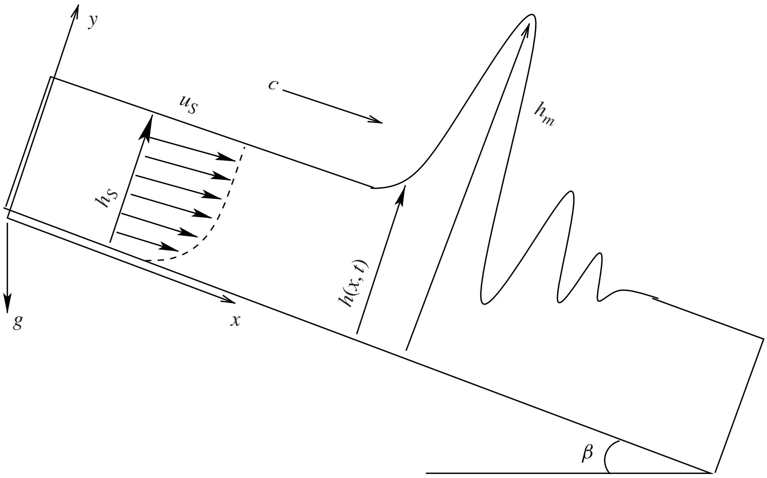

FIGURE 1. A sketch of the geometry for a Newtonian film flowing down an inclined plane.

components u and v in the x and y directions respectively. The liquid is incompressible and Newtonian, with density ρ, dynamic and kinematic viscosities μ and $\nu = \mu/\rho$, and surface tension σ. The elevation of the free surface is denoted by $h(x, t)$.

We consider stationary solitary-wave solutions, that is waves with fully developed shapes travelling at a constant phase speed c, whose main attribute is the localization of the deformation, so that the Nusselt flat-film solution of thickness h_S (subscript S denotes undisturbed film thickness) is asymptotically recovered at $x \to \pm\infty$. The characteristic velocity and thickness of the Nusselt flat-film solution at the back or front of the solitary wave form a natural choice of scales for the non-dimensionalization of the equations. The undisturbed film thickness h_S and mean velocity u_S are defined by

$$h_S = \left(\frac{3\mu Q}{\rho g \sin\beta}\right)^{1/3} \quad \text{and} \quad u_S = \frac{Q}{h_S} = \frac{g h_S^2 \rho \sin\beta}{3\mu} \tag{2.1}$$

where Q is the flow rate of the undisturbed film far away from the main hump. However, it is convenient to substitute $V \equiv \mathrm{d}Q/\mathrm{d}h_S = 3u_S$ for u_S as the velocity scale, because $\mathrm{d}Q/\mathrm{d}h_S$ is the speed of linear waves propagating at the surface of the Nusselt flow in the long-wave limit (Samanta, Ruyer-Quil & Goyeau 2011; Kalliadasis *et al.* 2012).

The dimensionless governing equations consist of the continuity and Navier–Stokes equations

$$\nabla \cdot \boldsymbol{u} = 0, \tag{2.2a}$$

$$\frac{\partial \boldsymbol{u}}{\partial t} + (\boldsymbol{u} \cdot \nabla)\,\boldsymbol{u} = -\nabla p + \frac{1}{3Re}\nabla^2 \boldsymbol{u} + \frac{1}{Fr^2}(\tan\beta, -1)^{\mathrm{T}}, \tag{2.2b}$$

complemented by the no-slip and no-penetration boundary conditions at the wall

$$u = v = 0 \quad \text{at } y = 0, \tag{2.2c}$$

and the kinematic and dynamic boundary conditions at the free surface

$$\frac{\partial h}{\partial t}+\boldsymbol{u}\frac{\partial h}{\partial x}-\boldsymbol{v} = 0 \quad \text{at } y=h, \tag{2.2d}$$

$$\boldsymbol{n}\cdot\boldsymbol{\tau} = \left(p+\frac{K}{We}\right)\boldsymbol{n} \quad \text{at } y=h, \tag{2.2e}$$

where $K=-\nabla\cdot\boldsymbol{n}$ is the mean curvature of the free surface, $\boldsymbol{\tau}$ is the viscous stress tensor and $\boldsymbol{n}$ is the normal unit vector at the free surface that points towards the gas. As the gas is passive, its pressure is constant, and thus is set to zero and does not appear in (2.2*e*).

The dimensionless groups arising in the governing equations (2.2) are the Reynolds, Weber and Froude numbers, which are defined as follows:

$$Re=\frac{Q}{\nu}=\frac{u_S h_S}{\nu}, \quad We=\frac{\rho h_S V^2}{\sigma}, \quad Fr^2=\frac{V^2}{\rho g\cos\beta h_S}=\frac{3Re}{\cot\beta}, \tag{2.3}$$

and compare inertia, viscous, capillary and gravity forces. As usual the Reynolds number is defined based on the averaged velocity u_S, which introduces a factor $3=V/u_S$ at various places in (2.2).

The traditional set of dimensionless numbers Re, We and Fr^2 has the disadvantage that all of them depend on the flow rate, which is the experimentally controlled variable. In practice, it can thus be useful to introduce instead of We the Kapitza number, $\varGamma$, defined as

$$\varGamma=(3Re)^{5/3}\,(We)^{-1}=\frac{\sigma}{\rho\nu^{4/3}(g\,\sin\beta)^{1/3}}, \tag{2.4}$$

or its variant, $\varGamma^*$

$$\varGamma^*=\varGamma\,(\sin\beta)^{1/3}=\frac{\sigma}{\rho\nu^{4/3}g^{1/3}}, \tag{2.5}$$

which is independent of inclination angle and only depends on liquid properties.

Finally, all the aforementioned dimensionless numbers may be recast as ratios of the characteristic lengths of the problem, i.e. the undisturbed film thickness, h_S, the capillary length $l_c = [(\sigma/(\rho g\,\sin\,\beta)]^{1/2}$ and a viscous–gravity length, $l_\nu=(\nu^2/(g\sin\beta))^{1/3}$ as follows

$$Re=\frac{1}{3}\left(\frac{h_S}{l_\nu}\right)^3, \quad \varGamma=\left(\frac{l_c}{l_\nu}\right)^2, \quad We=\left(\frac{l_\nu}{l_c}\right)^2\left(\frac{h_S}{l_\nu}\right)^5. \tag{2.6}$$

3. Dynamical systems approach

In this section we first recall the results that have been gained on the characteristics of solitary waves using low-dimensional models within the framework of the theory of dynamical systems.

3.1. *Shkadov's scales*

Solitary waves travel at a constant speed and shape. They remain stationary in their moving frame with coordinate $\xi = x - ct$. This change of coordinates transforms the set of partial differential equations, that form low-dimensional models of the flow, into an ordinary differential problem, which is then recast as an autonomous dynamical system. Every one-equation or two-equation model that has been proposed in the literature to deal with the nonlinear dynamics of falling liquid films yields dynamical systems in the phase space spanned by the film thickness h and its derivatives $h' \equiv \mathrm{d}h/\mathrm{d}\xi$ and $h'' \equiv \mathrm{d}^2h/\mathrm{d}\xi^2$ (Kalliadasis *et al.* 2012, Chapter 7). As stressed by Ruyer-Quil & Manneville (2005) and Ruyer-Quil & Kalliadasis (2012), it is advisable to adopt Shkadov's scaling (Shkadov 1977) and introduce different length scales for the streamwise and cross-stream directions. The appropriate length scale in the cross-stream direction is the undisturbed film thickness h_S, whereas the length scale in the streamwise direction κh_S is stretched by a factor $\kappa = \left[\sigma/(\rho g \sin\beta h_S^2)\right]^{1/3} = (l_c/h_S)^{2/3}$ which corresponds to the balance of the capillary pressure gradient $\propto \sigma \partial_{xxx} h$ and the gravity acceleration $g \sin\beta$ in the flow direction. This change of scales introduces two subsidiary dimensionless parameters, a 'reduced Reynolds number'

$$\delta \equiv 3Re/\kappa = (3Re)^{11/9} \Gamma^{-1/3} \tag{3.1a}$$

and a viscous dispersion parameter

$$\eta \equiv 1/\kappa^2 = \left(\frac{h_S}{l_c}\right)^{4/3} = (3Re)^{4/9} \Gamma^{-2/3}. \tag{3.1b}$$

The reduced Reynolds number δ compares inertia and viscous effects at the scale κh_S imposed by the balance of gravity and surface tension. The viscous diffusion parameter η is recast in (3.1*b*) in terms of the length ratio h_S/l_c. Thus, it compares capillary to viscous effects, and more specifically it measures the efficiency of the damping of short waves by viscous diffusion as compared to the damping by surface tension. Its christening as a dispersion parameter arises from the analysis of the primary stability of the flow within the frame of Whitham's wave hierarchy (Whitham 1974; Alekseenko *et al.* 1985; Ooshida 1999) that is allowed by two-equation models. Within that frame, the instability arises from the competition between lower-order waves, i.e. kinematic waves that are generated by the slaving of the velocity distribution to the deformation of the free surface through the kinematic boundary condition, and higher-order waves, or dynamic waves, i.e. surface gravity waves advected by the flow. The instability results from the inability of the kinematic waves to travel at a speed ($\approx 3u_S$) within the range allowed by dynamic waves ($\approx 0.8u_S \pm \sqrt{gh_S \cos\beta}$) whenever the inclination of the wall is too large, or equivalently whenever the flow velocity u_S is much larger than the speed of gravity waves $\sqrt{gh_S \cos\beta}$ which is formalized by the critical Froude number $Fr_c^{-2} = 2/5$. Ruyer-Quil *et al.* (2008) showed that the viscous damping of the short waves results from the dependence of the kinematic wave speed on ηk^2, k referring to the wavenumber, that is introduced by viscous effects.

One advantage of Shkadov's scaling is to reduce the set of parameters (δ, η, Fr^2) by one whenever surface tension damping of short waves overcomes viscous damping ($\eta \to 0$) which is a common situation for usual fluids such as water or alcohol corresponding to large Kapitza numbers ($\Gamma^* \approx 3400$ and 500 respectively). For these fluids, the capillary length l_c is much larger than the viscous–gravity length and therefore much larger than the undisturbed film thickness h_S for the range of Reynolds numbers ($Re \lessapprox 300$) at which a laminar wavy regime is reported. A second advantage is to combine into a single parameter – the reduced Reynolds number – inertia, viscosity and surface tension effects.

3.2. *One- and two-equation models*

Written using Shkadov's scaling, low-dimensional models of the dynamics of falling film flows can all be recast in the generic form

$$\partial_t h + \partial_x q = 0, \tag{3.2a}$$

$$q = \frac{1}{3}h^3\left(1 - \frac{\delta}{Fr^2}\partial_x h + \partial_{xxx} h\right) + \mathscr{Q}, \tag{3.2b}$$

where (3.2*a*) expresses the exact conservation of mass and relates the evolution of the film thickness h to the local flow rate $q \equiv \int_0^h u\,\mathrm{d}y$. Setting $\mathscr{Q}$ to zero, (3.2*b*) corresponds to flow generated by the acceleration due to gravity and by the capillary and hydrostatic pressure gradients. In the case of one-equation models such as the Benney equation (Gjevik 1970) or the Ooshida equation (Ooshida 1999), $\mathscr{Q}$ is a function of h and its partial derivatives only, whereas for two-equation models, $\mathscr{Q}$ is a function of h, and q and their derivatives. More complex models such as the four-equation model derived in Ruyer-Quil & Manneville (2000) can also be recast in the format (3.2) with $\mathscr{Q}$ being a function of h, q and two other amplitudes s_1 and s_2 whose evolutions are prescribed by two supplementary equations (see (3.16) below).

Considering travelling-wave (TW) solutions in the co-moving frame $\xi = x - ct$, (3.2*a*) satisfies $q' - ch' = 0$ whose integration gives

$$q = ch + q_0, \tag{3.3}$$

where $q_0 \equiv \int_0^h (u - c)\mathrm{d}y$ refers to the constant flow rate in the co-moving frame of reference. As a consequence, TW solutions to one-equation and two-equation models satisfy a single ordinary differential equations (ODE) for h after substitution of h for q into (3.2*b*). Neglecting for convenience second-order inertial corrections ($\propto \delta^2$), this ODE is

$$\frac{1}{3}h^3(1 + h''') - q + \delta\left(\mathscr{N}(h, c) - \frac{h^3}{3Fr^2}\right)h' + \eta\left[\mathscr{I}(h, c)\left[h'\right]^2 + \mathscr{J}(h, c)\,h''\right] = 0. \tag{3.4}$$

The expressions for the functions $\mathscr{N}$, $\mathscr{I}$ and $\mathscr{J}$ are given below for the one-equation model derived by Ooshida (1999) using a Padé-like regularization technique, and for the two-equation models formulated by Roberts (1996) and Ruyer-Quil & Manneville (2000) employing the tools of centre manifold analysis and a Galerkin weighted-residual technique (the latter being referred to hereinafter as weighted-residual integral boundary layer model, or WRIBL model):

$$\text{Ooshida:}\quad \mathscr{N} = \tfrac{10}{21}ch^4 - \tfrac{12}{35}h^6, \quad \mathscr{I} = 0, \quad \mathscr{J} = -ch^2, \tag{3.5}$$

$$\text{Roberts:}\quad \left.\begin{aligned} &\mathscr{N} = 0.405c^2h^2 - 1.015chq + 0.550q^2 + \tfrac{1}{1000}\left(3.235ch^4 + 6.999h^3q\right),\\ &\mathscr{I} = 1.402q - 1.359ch, \quad \mathscr{J} = -1.895qh + 1.659ch^2, \end{aligned}\right\} \tag{3.6}$$

$$\text{WRIBL model:}\quad \left.\begin{aligned} &\mathscr{N} = \tfrac{2}{5}c^2h^2 - \tfrac{34}{35}chq + \tfrac{18}{35}q^2 \approx 0.4c^2h^2 - 0.971chq + 0.514q^2,\\ &\mathscr{I} = 1.6q - 1.8ch, \quad \mathscr{J} = -2.4qh + 1.8ch^2. \end{aligned}\right\} \tag{3.7}$$

The ODE (3.4) can easily be recast as an autonomous dynamical system in the phase space spanned by h, h' and h''. Solitary-wave solutions correspond to homoclinic orbits in the phase space connecting a fixed point to itself (Pumir *et al.* 1983). Here we restrict ourselves to consider only single-loop homoclinic orbits connecting the fixed point $\boldsymbol{h}_I = (1, 0, 0)^{\mathrm{T}}$ and corresponding to single-hump solitary waves in real space. Ooshida (1999) analysed the structure of the tails of the solitary waves by considering how the homoclinic orbit escapes the fixed point (back tail) and returns to it (front tail). The homoclinic orbit being tangent to the linear stable and unstable sub-spaces when approaching the fixed point, it is possible to approximate the tails of the waves as $h - 1 = \mathrm{Re}[A \exp(\lambda \xi)]$, where Re signifies the real part and λ is a solution to the dispersion relation

$$\lambda^3 + \lambda^2 \eta D_\eta + \lambda \delta D_\delta - 3\,(c-1) = 0, \tag{3.8}$$

with $D_\eta = 3\mathscr{J}(1, c)$ and $D_\delta = 3\mathscr{N}(1, c) - Fr^{-2}$. The leading real eigenvalue is denoted by $\lambda_1 > 0$. The two other eigenvalues λ_2 and λ_3 have negative real parts and are generally complex.

Ooshida reported two different regimes corresponding to different behaviours of the tail lengths $l_{tail} = 1/|\mathrm{Re}(\lambda)|$ and of the speed c and maximum height of the waves. At low values of δ, the front and back tails of the waves have the same characteristic lengths with $l_{tail} \sim \delta^{-1/2}$, whereas at large values of δ, a separation of scales occurs with a (downstream) front tail far steeper ($l_{tail} \sim \delta^{-1/2}$) than the back one $l_{tail} \sim \delta$.

In the *drag–gravity regime*, that is in the vicinity of the instability threshold, $\left(1 - (5/2)Fr^{-2}\right)\delta \ll 1$ holds. Thus, the streamwise gravitational acceleration is mainly balanced by the viscous drag so that the character of the flow is close to that of the Nusselt flat-film solution, with both inertia and surface tension playing effectively a merely ‘perturbative’ role throughout the wave. The amplitude of the waves is small which allows a weakly nonlinear analysis of the waves ($h - 1 \ll 1$) from which the asymptotic behaviour of the amplitude and speed of the waves can be obtained in the vicinity of the instability threshold (Ruyer-Quil & Kalliadasis 2012):

$$\left.\begin{aligned} c &\approx 1 + 0.102\left[\left(1 - \tfrac{5}{2}Fr^{-2}\right)\delta\right]^{3/2} \\ h_{max} &\approx 1 + 0.132\left[\left(1 - \tfrac{5}{2}Fr^{-2}\right)\delta\right]^{3/2} \\ h_{max} &\approx 1 + 1.29(c-1). \end{aligned}\right\} \tag{3.9}$$

This asymptotic result is satisfied by every consistent model at first-order in the film parameter, in particular by the Ooshida equation, and the Roberts and WRIBL two-equation models.

The *drag–inertia* regime is characterized by an asymmetry of the wave shape following a sharp steepening of the front tail. At the upstream back tail of the wave, inertia balances wall drag and gravitational acceleration, surface tension is negligible and the flow is slowly varying with a small characteristic length $l_{tail} = 1/\lambda_1 \sim \delta$. At the downstream front tail, the steepening of the wave is arrested by surface tension or viscous diffusion which gives $l_{tail} = 1/\lambda_1 \sim 1/\max(\delta^{-1}, \eta)$ (Ruyer-Quil & Kalliadasis 2012). Focusing on the back tail, let us introduce a slow variable $\tilde{\xi} = \xi/\delta$:

$$\left(3\mathscr{N}(h, c) - \frac{h^3}{Fr^2}\right)\frac{\mathrm{d}h}{\mathrm{d}\tilde{\xi}} = 3q - h^3 + O(\eta/\delta^2, \delta^3). \tag{3.10}$$

The zeros of the right-hand side of (3.10) coincide with the locations of the fixed points in the phase space which are given by $h_I = 1$ and $h_{II} = -1/2 + \sqrt{3(c - 1/4)}$. As the film height reaches the level $h = h_{II}$, a maximum is attained if the left-hand side of (3.10) does not go to zero simultaneously, the resulting orbit being an heteroclinic orbit connecting the two fixed points. As a consequence, the construction of a one-loop homoclinic orbit then requires that the location of the second fixed point coincides with the location of a critical layer $h=h_c$ satisfying

$$3\mathscr{N}(h_c,c)-h_c^3 Fr^{-2}=0. \tag{3.11}$$

The asymptotic speed $c_\infty(Fr^{-2}) = \lim_{\delta\to\infty} c$ of the waves is thus given by the solution to

$$h_c(c,Fr^{-2})=h_{II}(c), \tag{3.12}$$

which is nothing but the Thomas condition derived in the context of the mathematical treatment of periodic bores, or roll waves consisting of regular sections of laminar flows connected by hydraulic jumps (Thomas 1939; Liu *et al.* 2005); $c_\infty(Fr^{-2})$ is a monotonic decreasing function which satisfies $c_\infty(Fr_c^{-2}=2/5)=1$. The maximum of the solitary-wave speed is reached at $Fr^{-2}=0$, i.e. for a vertical wall, and varies significantly with the specific model as is observed with the different models considered so far (Ruyer-Quil & Manneville 2005):

$$\text{Ooshida:}\quad c_\infty(0) = \tfrac{9}{841}\left(83+5\sqrt{141}\right)\approx 1.524, \tag{3.13}$$

$$\text{Roberts:}\quad c_\infty(0) \approx 2.982, \tag{3.14}$$

$$\text{WRIBL model:}\quad c_\infty(0) = \tfrac{1}{6}\left(9+\sqrt{43+2\sqrt{37}}\right)\approx 2.738. \tag{3.15}$$

3.3. *WRIBL four-equation model*

In the remainder of this section, we extend to more elaborate models the analysis of the characteristics of solitary waves in the drag–gravity and drag–inertia regimes proposed by Ooshida (1999) and Ruyer-Quil & Manneville (2005), Ruyer-Quil & Kalliadasis (2012). The four-equation WRIBL model derived by Ruyer-Quil & Manneville (2000) can be formally written

$$\begin{aligned}\delta\left\{\partial_t \boldsymbol{A}+\left(\frac{q\partial_x h}{h^2}\boldsymbol{M}_h+\frac{\partial_x q}{h}\boldsymbol{M}_q\right)\boldsymbol{A}+\frac{q}{h}\boldsymbol{M}_A\partial_x\boldsymbol{A}+\frac{h}{Fr^2}\partial_x h\boldsymbol{V}_b\right\}&\\ =h\left(1+\partial_{xxx}h\right)\boldsymbol{V}_b-h^{-2}\boldsymbol{M}_w\boldsymbol{A}+\eta\boldsymbol{M}_\eta\boldsymbol{B},&\end{aligned} \tag{3.16a}$$

where $\boldsymbol{A}=(q,s_1,s_2)$ is the amplitude vector and $\boldsymbol{M}_h$, $\boldsymbol{M}_q$, $\boldsymbol{M}_A$ and $\boldsymbol{V}_b$ are defined by

$$\boldsymbol{M}_h=\begin{bmatrix}-\dfrac{6}{5} & \dfrac{12}{5} & \dfrac{126}{65}\\ \dfrac{3}{35} & -\dfrac{108}{55} & \dfrac{5022}{5005}\\ 0 & \dfrac{4}{11} & -\dfrac{18}{11}\end{bmatrix},\quad \boldsymbol{M}_q=\begin{bmatrix}\dfrac{12}{5} & -\dfrac{12}{5} & -\dfrac{171}{65}\\ -\dfrac{1}{35} & \dfrac{103}{55} & -\dfrac{9657}{5005}\\ 0 & \dfrac{2}{33} & \dfrac{19}{11}\end{bmatrix}, \tag{3.16b}$$

$$\boldsymbol{M}_A=\begin{bmatrix}0 & -\dfrac{12}{5} & -\dfrac{1017}{455}\\ 0 & \dfrac{39}{55} & -\dfrac{10557}{10010}\\ 0 & -\dfrac{6}{55} & \dfrac{288}{385}\end{bmatrix},\quad \boldsymbol{M}_w=\begin{bmatrix}\dfrac{81}{28} & 33 & \dfrac{3069}{28}\\ \dfrac{3}{10} & \dfrac{126}{5} & \dfrac{126}{5}\\ \dfrac{13}{140} & \dfrac{39}{5} & \dfrac{11817}{140}\end{bmatrix},\quad \boldsymbol{V}_b=\begin{bmatrix}\dfrac{27}{28}\\ \dfrac{1}{10}\\ \dfrac{13}{420}\end{bmatrix}. \tag{3.16c}$$

The viscous terms $\eta \boldsymbol{M}_\eta \boldsymbol{B}$ are defined by $\boldsymbol{B} = \left(q\,(\partial_x h)^2/h^2,\ \partial_x q \partial_x h/h,\ \partial_{xx} q\right)$ and

$$\boldsymbol{M}_\eta = \begin{bmatrix} \dfrac{5025}{896} & -\dfrac{5055}{896} & -\dfrac{10851}{1792} & \dfrac{2027}{448} \\ \dfrac{93}{40} & -\dfrac{69}{40} & \dfrac{21}{80} & -\dfrac{9}{40} \\ -\dfrac{3211}{4480} & \dfrac{2613}{4480} & -\dfrac{2847}{8960} & \dfrac{559}{2240} \end{bmatrix}. \tag{3.17}$$

Considering travelling-wave solutions, the four-equation system (3.16) is recast into a dynamical system of dimension five in a phase space spanned by h, h', h'', s_1 and s_2. Turning to the solitary waves in the drag–inertia regime, our computations show that solutions to the four-equation models present again a slowly varying tail $l_{tail} \sim \delta$. Focusing on the back tail and using a squeezed coordinate system $\tilde{\xi} = \xi/\delta$, the five-dimensional dynamical system corresponding to (3.16) then reduces to a three-dimensional one

$$\boldsymbol{M}\frac{\mathrm{d}\boldsymbol{X}}{\mathrm{d}\tilde{\xi}} = \boldsymbol{B} + O\left(\eta/\delta^2, \delta^{-3}\right), \tag{3.18a}$$

where $\boldsymbol{X} = (h, s_1, s_2)^t$, and $\boldsymbol{M} = [\boldsymbol{M}_i]$ is a matrix whose column vectors are denoted by $\boldsymbol{M}_i$. The expressions for the vectors $\boldsymbol{M}_i$ and $\boldsymbol{B}$ are

$$\boldsymbol{M}_1 = \begin{bmatrix} -c^2 + \dfrac{27}{28}\dfrac{h}{Fr^2} + c\left(\dfrac{12}{5}\dfrac{q}{h} - \dfrac{12}{5}\dfrac{s_1}{h} - \dfrac{171}{65}\dfrac{s_2}{h}\right) + \dfrac{q}{h^2}\left(\dfrac{12}{5}s_1 + \dfrac{126}{65}s_2\right) - \dfrac{6}{5}\dfrac{q^2}{h^2} \\ c\left(-\dfrac{1}{35}\dfrac{q}{h} + \dfrac{103}{55}\dfrac{s_1}{h} - \dfrac{9657}{5005}\dfrac{s_2}{h}\right) + \dfrac{q}{h^2}\left(-\dfrac{108}{55}s_1 + \dfrac{5022}{5005}s_2\right) + \dfrac{3}{35}\dfrac{q^2}{h^2} \\ c\left(+\dfrac{2}{33}\dfrac{s_1}{h} + \dfrac{19}{11}\dfrac{s_2}{h}\right) + \dfrac{q}{h^2}\left(\dfrac{4}{11}s_1 - \dfrac{18}{11}s_2\right) \end{bmatrix}, \tag{3.18b}$$

$$\boldsymbol{M}_2 = \begin{bmatrix} -\dfrac{12}{5}\dfrac{q}{h} \\ \dfrac{39}{55}\dfrac{q}{h} - c \\ -\dfrac{6}{55}\dfrac{q}{h} \end{bmatrix}, \quad \boldsymbol{M}_3 = \begin{bmatrix} -\dfrac{1017}{455}\dfrac{q}{h} \\ -\dfrac{10557}{10010}\dfrac{q}{h} \\ \dfrac{288}{385}\dfrac{q}{h} - c \end{bmatrix}, \tag{3.18c}$$

$$\boldsymbol{B} = \begin{bmatrix} \dfrac{27}{28}h - \dfrac{81}{28}\dfrac{q}{h^2} - 33\dfrac{s_1}{h^2} - \dfrac{3069}{28}\dfrac{s_2}{h^2} \\ \dfrac{1}{10}h - \dfrac{3}{10}\dfrac{q}{h^2} - \dfrac{126}{5}\dfrac{s_1 + s_2}{h^2} \\ \dfrac{13}{420}h - \dfrac{13}{140}\dfrac{q}{h^2} - \dfrac{39}{5}\dfrac{s_1}{h^2} - \dfrac{11817}{140}\dfrac{s_2}{h^2} \end{bmatrix}. \tag{3.18d}$$

The shape of the back tail of the waves is determined, in the region of the fixed point, by the eigenvectors $\boldsymbol{X}_1$ corresponding to the smallest positive eigenvalue λ_1 solutions to the stability problem of the fixed point. Numerical computations of $\boldsymbol{X}_1$ show that, for all cases of interest, this eigenvector is nearly aligned with the unit vector $(1, 0, 0)^t$. We can therefore approximate the flow corresponding to the back tail of the waves by setting $s_1 \approx s_2 \approx 0$ in (3.18). This assumption reduces the five-dimensional dynamical system (3.18) to a three-dimensional one corresponding to (3.10) where $\mathscr{N}$ is given by

$$\mathscr{N} = \tfrac{28}{405}\left(5\,c^2h^2 - 12\,c\,h + 6\,q^2\right) \approx 0.346\,c^2h^2 - 0.830\,c\,h + 0.415\,q^2. \tag{3.19}$$

Within this assumption, an analytic expression for the asymptotic speed c_∞ of solitary waves can be found using (3.12). We thus obtain

$$c_\infty(Fr^{-2}) \approx 1 + \frac{1}{168\sqrt{\varDelta}}\left(168 + 2\varDelta\sqrt{\frac{42(56-405Fr^{-2}) - 196(\varDelta-9)\sqrt{\varDelta}}{\sqrt{\varDelta}}}\right), \tag{3.20a}$$

$$\varDelta = 3 + \left(\frac{2}{7\varUpsilon}\right)^{1/3}(14 - 405Fr^{-2}) + \frac{\varUpsilon^{1/3}}{2\times 14^{2/3}}, \tag{3.20b}$$

$$\begin{aligned}\varUpsilon = {} & 14112 + 10\,935Fr^{-2}(135Fr^{-2} - 56) \\ & + 5^{1/2}\left\{39\,337\,984 + 1215Fr^{-2}\left[-2\,809\,856 \right.\right. \\ & \left.\left. + 81Fr^{-2}(83\,4176Fr^{-2}(-5264 + 6561Fr^{-2}))\right]\right\}^{1/2}.\end{aligned} \tag{3.20c}$$

For a vertical plane ($Fr^{-2} = 0$), (3.20) simplifies to

$$c_\infty(0) \approx 1 + \frac{1}{\sqrt{6}}\sqrt{\frac{1}{2} + \sqrt{\frac{2}{3}}} \approx 2.555\,64. \tag{3.21}$$

Now, considering that s_1 and s_2 are small but not negligible and δ large but not infinite, we can expect from the previous analysis that the homoclinic orbit departing from the fixed point $h_{\mathrm{I}} = 1$ encounters a critical surface in the phase space at which the system (3.18) is not invertible, i.e. $\det \boldsymbol{M} = 0$. On the critical surface, the column vectors $\boldsymbol{M}_i$ are linearly dependent and thus $\boldsymbol{M}\mathrm{d}\boldsymbol{X}/\mathrm{d}\tilde{\xi}$ is a linear combination of $\boldsymbol{M}_2$ and $\boldsymbol{M}_3$ which yields $\mathscr{D} \equiv \det[\boldsymbol{B}, \boldsymbol{M}_2, \boldsymbol{M}_3] = O\left(\eta/\delta^2, \delta^{-3}\right)$. Denoting by $\boldsymbol{X}_c$ the first point of intersection of the homoclinic orbit with the critical surface and denoting by $\boldsymbol{X}_\infty$ its location in the limit $\delta \to \infty$, we have $\partial_{\boldsymbol{X}}\mathscr{D} \boldsymbol{\cdot} (\boldsymbol{X}_c - \boldsymbol{X}_\infty) = O\left(\eta/\delta^2, \delta^{-3}\right)$. Since one-humped homoclinic orbits are solutions to a nonlinear eigenproblem for the phase speed c, $|\boldsymbol{X}_c - \boldsymbol{X}_\infty| \propto c - c_\infty$ and we thus obtain

$$c - c_\infty = O\left(\eta/\delta^2, \delta^{-3}\right). \tag{3.22}$$

Surface tension effects on the shape of the tails of extreme solitary wave are responsible for the $O(\delta^{-3})$ terms on the right-hand side of (3.22), whereas $O(\eta/\delta^2)$ terms arise from streamwise viscous diffusion. Since $\eta/\delta^2 = 1/(3Re)^2 = \varGamma^{-6/11}\delta^{-18/11}$ varies as $\delta^{-18/11}$ for a given Kapitza number, the convergence of c to its asymptotic value c_∞ is eventually driven by viscous diffusion terms and not by surface tension.

4. Computational methodology

4.1. *Finite-element formulation*

We now turn to the numerical computation of solitary-wave solutions to the governing equations (2.2). As in § 2, we consider travelling waves that are stationary in their co-moving frame $\xi = x - ct$. The solitary wave is assumed to travel on a base film which is undisturbed far away from the main hump. Thus, if the solitary hump is placed at the middle of a sufficiently large domain of length L, the liquid film near the inflow and outflow corresponds to the flat-film Nusselt solution.

The resulting equations are as follows:

$$\begin{aligned} \mathbb{C} &\equiv \nabla \boldsymbol{\cdot} \boldsymbol{u} = 0, && (4.1a) \\ \mathbb{M} &\equiv -c\frac{\partial \boldsymbol{u}}{\partial x} + (\boldsymbol{u} \boldsymbol{\cdot} \nabla)\,\boldsymbol{u} + \nabla p - \frac{1}{Re}\nabla^2 \boldsymbol{u} - \frac{1}{Fr^2}(\tan\beta,\, -1)^{\mathrm{T}}, && (4.1b) \end{aligned}$$

coupled with the kinematic equation for free-surface evolution

$$\mathbb{K} \equiv -c\frac{\partial h}{\partial x} + u\frac{\partial h}{\partial x} - v = 0, \qquad (4.1c)$$

where time derivatives are replaced by spatial derivatives according to $\partial_t = -c\partial_x$.

The no-slip and no-penetration boundary conditions (2.2*c*) at the wall and the dynamic boundary condition (2.2*e*) at the free surface are enforced, and the set of boundary conditions is completed by the requirement of periodicity, $X(L) = X(0)$, where X refers to any of the four variables u, v, p and h. So far (4.1) is a boundary-value problem with an eigenvalue c to be determined. An additional condition is obtained by setting the thickness of undisturbed film far away from the main hump

$$h(x=0) = 1. \qquad (4.2)$$

Finally, the translational invariance is prevented by pinning the maximum height of the wave at the middle of the domain

$$\frac{\partial h}{\partial x}(x = L/2) = 0. \qquad (4.3)$$

Using the Galerkin finite-element method on a structured grid, the system of governing equations is integrally weighted with bi-linear $\Psi^i(\theta,\, \varsigma)$ $(i = 1,\, 4)$, bi-quadratic $\Phi^i(\theta,\, \varsigma)$ $(i = 1,\, 9)$ and quadratic basic functions $\Phi^i(\theta,\, \varsigma = 1)$ $(i = 1,\, 3)$, to produce respectively the residuals of the continuity, momentum and kinematic equations,

$$\begin{aligned} \iint_V \mathbb{C}\, \Psi^i(\theta,\, \varsigma)\, \mathrm{d}V &= 0, && (4.4a) \\ \iint_V \mathbb{M}\, \Phi^i(\theta,\, \varsigma)\, \mathrm{d}V &= \underline{0}, && (4.4b) \\ \int_S \mathbb{K}\, \Phi^i(\theta,\, \varsigma = 1)\, \mathrm{d}S &= 0, && (4.4c) \end{aligned}$$

where θ and ς are element-wise coordinates in each element of the computational domain. The flow field variables are interpolated from nodal unknowns using the same basis functions.

$$\boldsymbol{u} = \sum_{i=1,9} \boldsymbol{u}_i\, \Phi^i(\theta,\, \varsigma), \qquad (4.5a)$$

$$p = \sum_{i=1,4} p_i \Psi^i(\theta, \varsigma), \tag{4.5b}$$

$$h = \sum_{i=1,3} h_i \Phi^i(\theta, \varsigma = 1). \tag{4.5c}$$

The element-wise integration results in a discretized system of algebraic equations, which is solved by the Newton–Raphson iterative scheme using a frontal technique (Hood 1976) to invert the matrix.

4.2. *Mesh clustering*

Following a standard exponential mesh clustering technique (Hoffmann & Chiang 2000), the grid of the flow domain is refined in the streamwise direction in the vicinity of the main hump of the solitary wave, and relaxed in the nearly flat undisturbed film far away from the hump. To this end, the following transformations are used:

$$x = L\left\{1 + \frac{\sinh[\alpha(\theta - A)]}{\sinh(\alpha A)}\right\}, \tag{4.6a}$$

$$y = h(x)\,\varsigma, \tag{4.6b}$$

where

$$A = \frac{1}{2\alpha}\ln\left[\frac{1 + (\mathrm{e}^{\alpha} - 1)(x_m/L)}{1 + (\mathrm{e}^{-\alpha} - 1)(x_m/L)}\right], \tag{4.6c}$$

α is a clustering parameter in the range of $0 < \alpha < \infty$ and $x = x_m$ refers to the location of maximum clustering, which is here taken as $x_m = L/2$, i.e. at the crest of the main hump. Physical coordinate y is not clustered, but only scaled with the free-surface height $h(x)$ in (4.6b).

The isoparametric mapping from the physical domain to a square computational domain of unit length is done by the transformations (4.6a) and (4.6b) where $0 < \theta < 1$ and $0 < \varsigma < 1$ (for brevity, the same notation is used here as for the coordinates in each element of the computational domain). The grid is Cartesian with constant step size $\Delta\theta$ and $\Delta\varsigma$. To ensure that the waves are truly localized, the characteristics of the waves, height h_m and speed c, are monitored and the domain extended until both c and h_m are independent of L. Accordingly, the clustering parameter α is selected such that the minimum space step Δx is much smaller than the scaled capillary length, i.e. $N_c\,\Delta x \leqslant l_c/h_S$, where a large factor $N_c = 512$ is empirically chosen.

5. Results

In the next subsections we present results of direct numerical simulation and discuss them in relation to asymptotic predictions of the models of reduced dimensionality. The goal is to assess the performance of currently available models and to select the most accurate among them. At the same time the DNS results may serve as a benchmark for future modelling efforts. Most results refer to a vertical wall ($\beta = 90^\circ$, $Fr^{-2} = 0$), in order to simplify the parametric dependence and also because this is the most studied situation in the literature. The parametric variation of the phase speed and height of travelling waves, i.e. waves that remain stationary in a co-moving reference frame, is investigated first. Solitary waves are obtained in the limit of

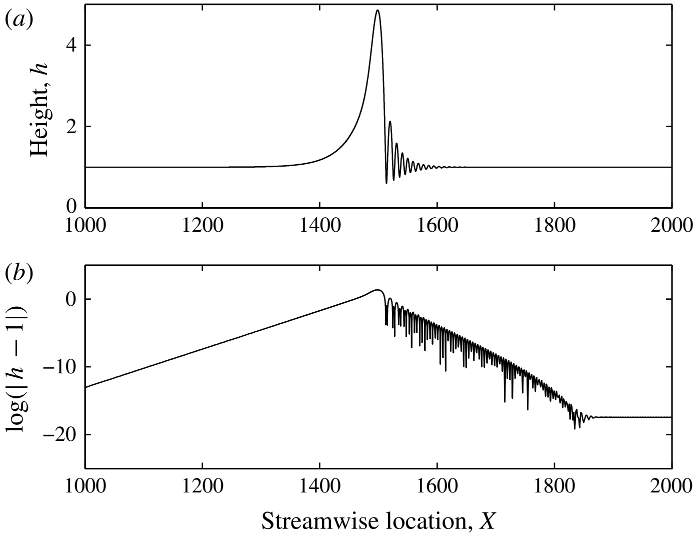

FIGURE 2. Free-surface profile of a solitary wave and its exponential representation at $\delta=4$, $\Gamma=3400$, $Fr^{-2}=0$. The extent of the computational domain is $L=3000$ and only the central part of it is represented.

a large computational domain, through an homoclinic bifurcation (see for instance Chang & Demekhin 2002). Next, the shape of the wave is studied in more detail, in particular the steepness with which the profile declines towards the undisturbed film. Then, the structure of the flow is examined, concentrating on the phenomenon of backflow. Finally, the effect of non-vertical wall inclination is considered.

5.1. *Wave phase speed and height*

Figure 2 shows the profile of a one-hump solitary wave obtained by DNS for $\Gamma=3400$ and $\delta=4$. The full extent of the computational domain is $L=3000$ and only the central one-third of it is presented. It is observed that the wave profile converges to the Nusselt flat-film solution ($h=1$) far from the hump, i.e. that true homoclinicity is achieved. Also, particular attention has been paid to the variation of the characteristics of the wave (speed and amplitude) with respect to the domain extent L, the value $L=3000$ being selected to ensure that these characteristics are no longer affected by L. The same data are replotted in semi-log coordinates (figure 2*b*), and confirm the exponential decline of the back tail of the wave. Similarly, the envelope of the oscillatory decay of the front tail is observed to follow an exponential rule. These observations are in qualitative agreement with the asymptotic prediction of (3.8). Actual eigenvalues (exponents of decline) are compared in the next subsection.

The phase speed and the height of stationary waves are displayed in figures 3(*a*) and 3(*b*) as functions of the reduced Reynolds number δ, and as directly related to each other in figure 3(*c*). Results are presented for three different values of the Kapitza number: $\Gamma=193$ corresponds to a water–glycerol solution, $\Gamma=3400$ to plain water and $\Gamma=10\,000$ to liquid nitrogen. The last value is indicative of the high-Γ limit. As δ increases from the critical value ($\delta=0$), the phase speed first grows very rapidly, then exhibits an inflection point growing further until a maximum value and finally drops to a plateau. The magnitude of the maximum varies with Γ, but the low-δ and high-δ regions appear not to depend on it.

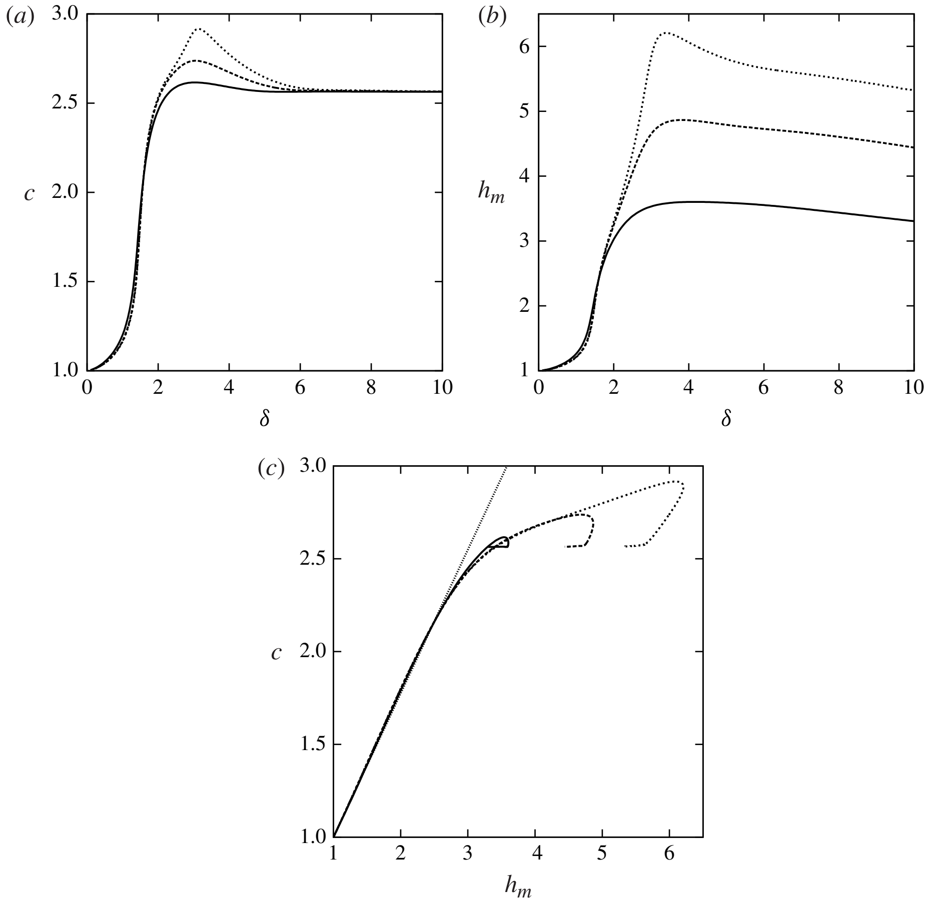

FIGURE 3. (*a*) Speed c and (*b*) amplitude h_m of solitary waves versus δ for a vertical wall and different Kapitza numbers: $\varGamma = 193$ (solid line), $\varGamma = 3400$ (dashed line) and $\varGamma = 10\,000$ (dotted line). (*c*) The same data plotted as h_m versus c, and compared to the asymptotic law (3.9) (thin-dotted line).

The wave height, h_m, exhibits a similar rapid growth at small δ, followed by an inflection point leading to a maximum value. With further increase in δ, the wave height saturates and starts to decrease slowly, and this trend continues up to the largest δ tested. The slow decrease of the wave height deep in the drag–inertia regime may be understood in physical terms by reverting to dimensional variables. As was experimentally observed by Karapantsios, Paras & Karabelas (1989), further increase in the liquid flow rate at high *Re* does not alter the dimensional height of the waves but only increases the dimensional undisturbed film thickness. Thus, in the scaling of the present work the dimensionless height h_m decreases, and further inertia is no longer balanced by capillarity (i.e. higher ripples) but only by drag at the wall. As for the dependence of h_m on $\varGamma$, figure 3(*b*) shows that the low-δ region is independent of $\varGamma$, but the maximum in height and the high-δ region depend on it. In particular, the maximum height of the solitary waves, as well as the maximum amplitude of the front-running capillary ripples, are strongly increasing functions of $\varGamma$.

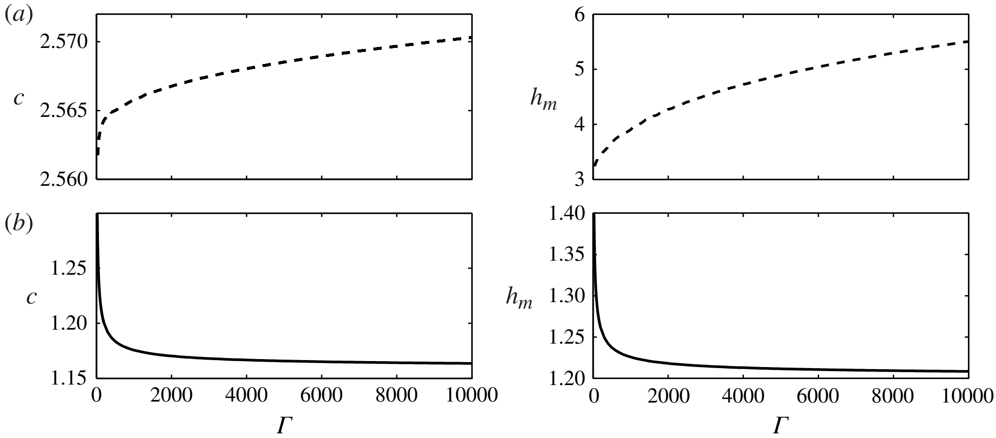

FIGURE 4. Solitary-wave speed and amplitude versus Kapitza number Γ for a vertical wall. (*a*) Dashed lines: $\delta = 8$ drag–inertia regime. (*b*) Solid lines: $\delta = 1$ drag–gravity regime.

Based on figures 3(*a*) and 3(*b*), the parametric regimes of solitary waves may be defined quantitatively. More specifically, the drag–gravity regime is bracketed from above by $\delta \approx 1.4$ ($c \approx 1.5$, $h_m \approx 1.8$). In this regime, h_m and c are linearly related as is exhibited in figure 3(*c*). However, the asymptotic laws (3.9) provide an accurate description only in a much narrower range sufficiently close to $\delta = 0$. The intermediate regime of δ corresponds to the neighbourhood of the maxima in phase speed and wave height. Not only the magnitudes, but also the locations of these maxima vary with Γ. Furthermore, though they remain close to each other, the maximum in height does not occur at exactly the same Γ as the maximum in phase speed. The drag–inertia regime is associated with the attainment by the phase speed of the plateau value. Thus, figure 3(*a*), indicates that it is bracketed from below by $\delta \approx 6$. The observed independence of c from Γ is in accord with the asymptotic analysis of the drag–inertia regime based on low-dimensional models and summarized in § 3 (Thomas condition). It is recalled though, that different models lead to widely different predictions of c_∞. The behaviour of the wave height in the drag–inertia regime, i.e. the displacement of the h_m versus δ curve to higher values with increasing Γ, is a direct consequence of the role of viscous diffusion: viscous diffusion is stronger at low Γ, and thus stabilizes the waves at smaller heights.

Considering further the effect of Kapitza number – and with a view to extreme values – we present in figure 4 the parametric dependence on Γ of the wave speed and wave height for two representative cases, one in the drag–gravity regime ($\delta = 1$) and one in the drag–inertia regime ($\delta = 8$). In the drag–inertia regime, the wave speed c remains almost constant, whereas the wave amplitude increases significantly with Γ. The latter can be explained by a less effective viscous damping as $\eta = \delta^{4/11}\Gamma^{-6/11}$ decreases. In the drag–gravity regime, the speed and amplitude of the waves are nearly constant for sufficiently high values of Γ and follow closely (3.9). Yet, at very low Γ, a significant amplification of speed and height of the waves is observed, the origin of which can be traced back to the influence of Trouton second-order viscosity on the dispersion of the waves (Ruyer-Quil & Kalliadasis 2012).

With respect to modelling of the above parametric variation of phase speed and height of solitary waves with δ, it is noted that none of the two-equation

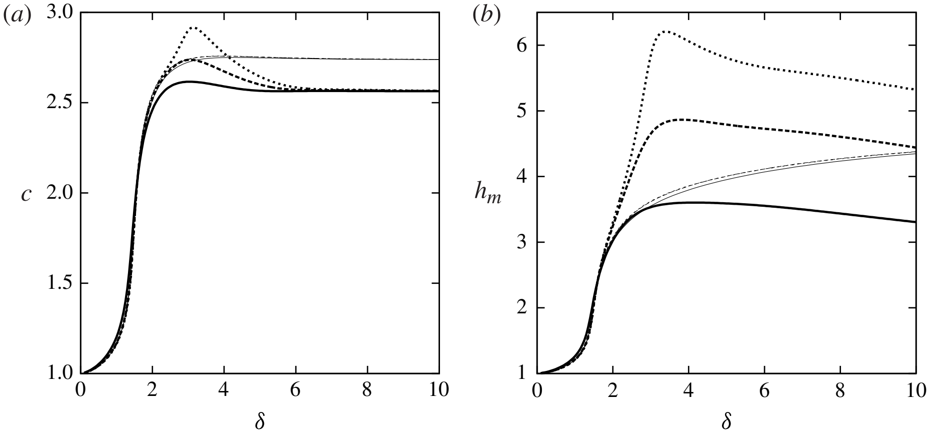

FIGURE 5. The DNS results of figure 3 (thick lines) are compared to predictions of the two-equation WRIBL model (thin lines).

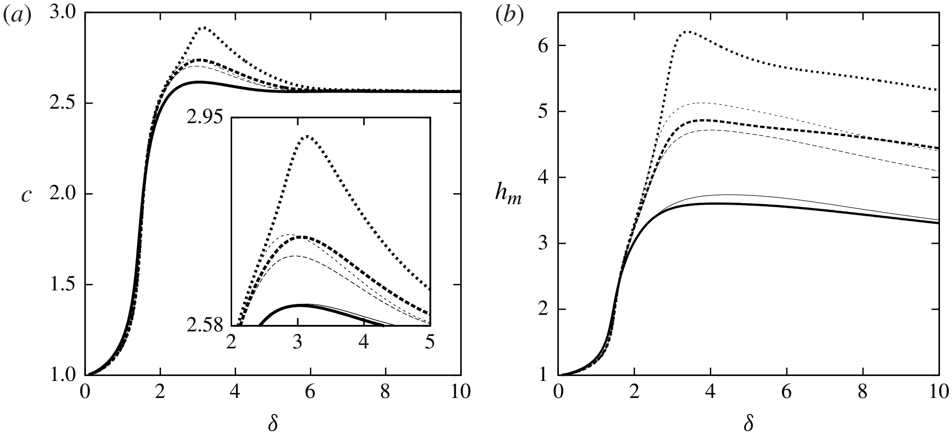

FIGURE 6. The DNS results of figure 3 (thick lines) are compared to predictions of the four-equation WRIBL model (thin lines).

models is capable of predicting the observed maxima, as they all exhibit monotonic dependence on δ. The two-equation WRIBL model does on average the best job, and its predictions are compared to DNS in figure 5. It is noted that the model provides roughly the same results for all three values of Γ tested, and thus fails to describe the effect of viscous diffusion. The predictions of the four-equation WRIBL model are compared to DNS in figure 6. This more involved model is found to describe satisfactorily all the trends in the parametric variation with δ, and in particular the inflection points and maxima at intermediate δ. Furthermore, the predictions of c and h_m vary significantly with Γ, and thus the effect of viscous diffusion is taken correctly into account. The relevant predictions are actually in quantitative agreement with DNS for $\Gamma = 193$ and $\Gamma = 3400$ and fail only at the highest $\Gamma = 10\,000$. As a consequence of the above comparisons, we concentrate in the rest of the paper on the four-equation WRIBL model.

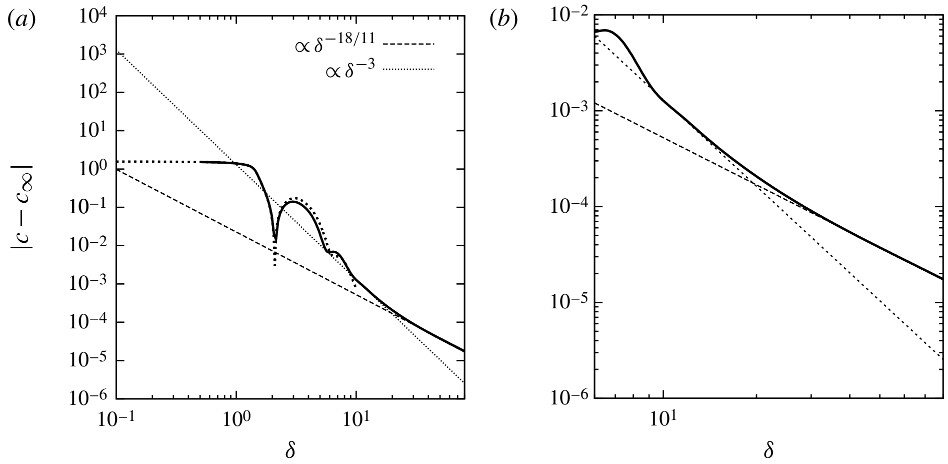

FIGURE 7. Convergence of the phase speed to its asymptotic value c_∞ for a vertical wall and $\Gamma = 3400$: thick solid line: four-equation model; thick dotted line: DNS. The high-δ limit of (*a*) is magnified in (*b*).

Model	c_∞
Ooshida	1.524
Roberts	2.982
WRIBL two-equation	2.738
Four-equation: simple	2.556
Four-equation: rigorous	2.564
DNS	2.560

TABLE 1. Prediction of c_∞ by various models and by DNS.

The prediction of the value of c_∞, the high-δ limit of the wave phase speed, provides another check of the low-dimensional models. Results of the two-equation models for a vertical film were derived at the end of § 3.2 and are reproduced in table 1, together with the simplified equation (3.21) and the rigorous prediction of the four-equation WRIBL model, and with the result of DNS. Compared to the result of DNS, the Ooshida model strongly underpredicts c_∞, the Roberts model overpredicts it and the two-equation WRIBL model overpredicts it but somewhat less. The four-equation model is in close agreement with DNS, and thus justifies its further consideration.

The last two data points in table 1 were derived numerically by exploiting the scaling rule of (3.22), and more specifically by positing a dependence of the form

$$c - c_\infty \approx A\,\eta/\delta^2 + B\,\delta^{-3}. \tag{5.1}$$

Treating c_∞, A and B as adjustable parameters, we may fit this equation to high-δ values of c, and thus calculate c_∞. The convergence of the phase speed c to its asymptotic value c_∞ is illustrated in figure 7(*a*), and the high-δ limit is magnified in figure 7(*b*).

5.2. *Tail lengths and shapes*

In this section, we specifically address the shape of the waves as they depart from the Nusselt film solution, that is their downstream and upstream tails. In these regions, it is possible to assume small deviations from the Nusselt solution, i.e. $X = X_0 + \varepsilon \mathrm{Re}(A\mathrm{e}^{\lambda(x-ct)})$ with $\varepsilon \ll 1$. Here X refers to the set of unknowns and X_0 to the Nusselt solution. Linearization of the governing equations leads to the classical Orr–Sommerfeld equations (see for instance Brevdo *et al.* 1999) with wavenumber and angular frequency given by $k = \lambda$ and $\omega = \lambda c$. We have solved the Orr–Sommerfeld eigenvalue problems by continuation using AUTO07P software (Doedel *et al.* 2007). The real eigenvalue $\lambda_1 > 0$ associated with the upstream tail and the pair of complex-conjugate eigenvalues $\lambda_{2,3} = \lambda_{2r} \pm \mathrm{i}\lambda_{2i}$ with $\lambda_{2r} < 0$ corresponding to the downstream tail have been computed starting from the marginal stability solutions to the Orr–Sommerfeld problem, that is $\lambda = 0$ and $c = 1$, and $\lambda = k_c$ and $c = \omega_c/k_c$ where k_c and ω_c define the marginal stability curve, and then adjusting c to the nonlinear phase speed of the considered solitary wave. Here $l_{tail} = 1/\lambda_1$ defines the characteristic length of the upstream tail of the wave, whereas $1/\lambda_{2i}$ characterizes the length of the radiation oscillations at the front of the solitary hump.

Figure 8 presents the results of our computations for the solitary-wave one-humped solutions at $\varGamma = 193$ and compares them to the predictions from the four-equation WRIBL model. Here λ_1 presents a maximum at $\delta \approx 1.4$ which signals the transition between the drag–gravity and the drag–inertia regimes (Ooshida 1999). Based on first-order models, i.e. when second-order viscous effects are disregarded ($\eta = 0$), Ooshida (1999) and Kalliadasis *et al.* (2012) suggested $\lambda_1 \propto \delta^{1/2}$ in the drag–gravity regime ($\delta \lessapprox 1.4$) and $\lambda_1 \propto \delta^{-1}$ in the drag–inertia regime ($\delta \gtrapprox 1.4$). These two asymptotic laws are tested against DNS data in figure 8(*a*). Small deviations can be noticed either when δ is very small or when δ becomes large. Considering the downstream tail of the waves, λ_{2r} and λ_{2i} are monotonic functions of the reduced Reynolds number δ. The asymptotic laws $\lambda_{2i} \propto \delta^{1/2}$ and $\lambda_{2r} \propto \delta^{1/2}$ are reasonably satisfied in the drag–gravity regime.

Comparisons with the solutions to the four-equation WRIBL model show a good agreement in the drag–gravity regime. However, results from DNS significantly depart from the model solutions when δ is larger than unity in the drag–inertia regime. In particular, the values of λ_{2r} computed by DNS are much larger than the predictions from the model, whereas, though some discrepancies are noticeable, our computations show a much better agreement in the case of λ_{2i} and λ_1. As a consequence, the upstream tail of the waves is accurately captured by the WRIBL model, whereas the front of the waves is only in qualitative agreement. Since the model grossly underestimates $|\lambda_{2r}|$, the attenuation of the capillary ripples in not well captured by the model which tends to overestimate their number.

5.3. *Flow reversal*

An interesting feature of wavy falling film flows is the occurrence of backflow, i.e. the appearance of regions where the streamwise velocity is locally negative and the flow is oriented against gravity. This feature was predicted by numerical computations (Malamataris *et al.* 2002; Dietze *et al.* 2008), and also by long-wave models (Scheid *et al.* 2006; Oron, Gottlieb & Novbari 2009). The onset of backflow may be detected experimentally by a change of sign in the wall shear stress (Tihon *et al.* 2006). This phenomenon was predicted to result in a significant enhancement of mass and heat transfer in the wall region, and was interpreted in terms of the oscillatory variation

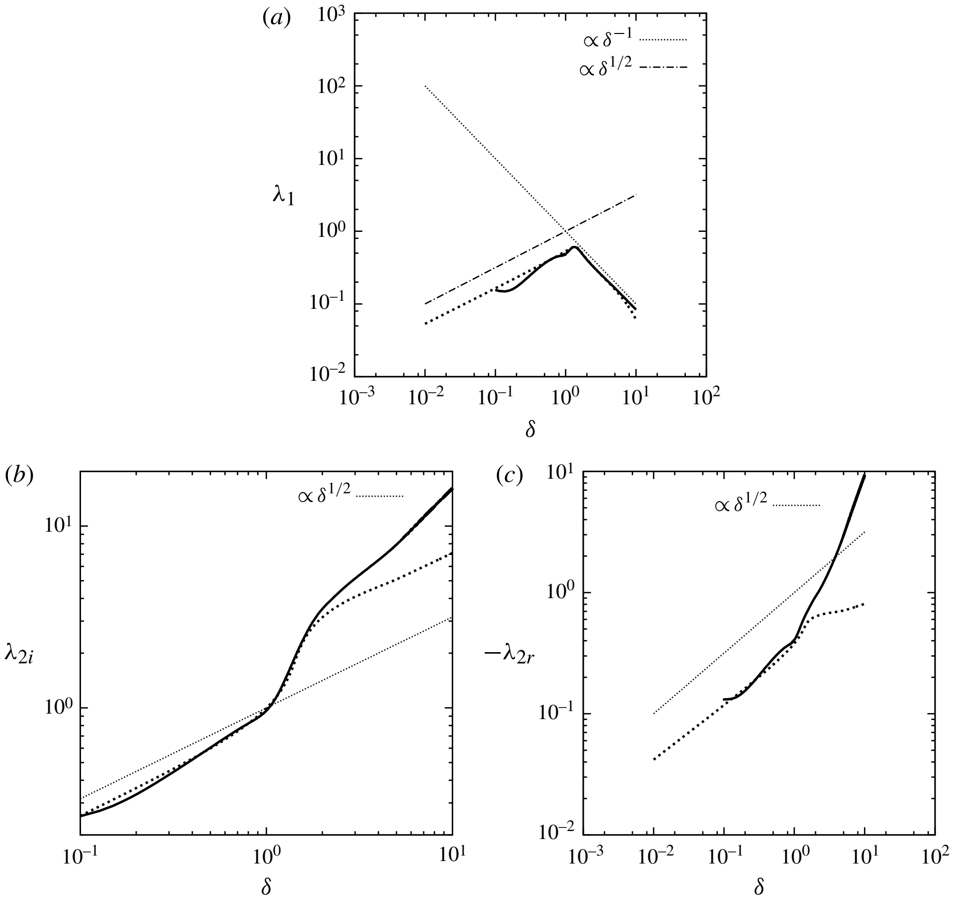

FIGURE 8. Tail eigenvalues of the solitary-wave solutions. (*a*) Real eigenvalue λ_1 corresponding to the upstream tail. (*b*) Imaginary part and (*c*) real part of complex eigenvalue λ_2 corresponding to the downstream tail. Solutions of the Orr–Sommerfeld problem (thick solid lines) are compared to the solutions of the four-equation WRIBL model (thick dotted lines).

of capillary pressure that is caused by the front-running ripples (Dietze *et al.* 2008). Because of surface tension and the local curvature of the free surface, a hump is a high-pressure region whereas a trough is a low-pressure one. Thus, strong pressure gradients are generated from the humps to the nearby troughs, which may overcome the gravitational acceleration and slow down the flow up to the reversal point.

The typical flow pattern in the capillary region of a wave is depicted in figure 9. The boundaries of the backflow regions are visualized by the isolines at which the streamwise velocity *u* goes to zero. Backflow regions are located at the local minima of the height, and are characterized by clockwise eddy-like structures whose upper part remains open. As a consequence, no closed streamlines are found and recirculation zones cannot be observed. Instead, a fluid particle located at the free surface will be alternately displaced forward and backward as the wave advances and the particle goes from one hump to the next trough. The motion is rather slow, as the local velocity is relatively small, until the particle reaches the wave crest, at which point

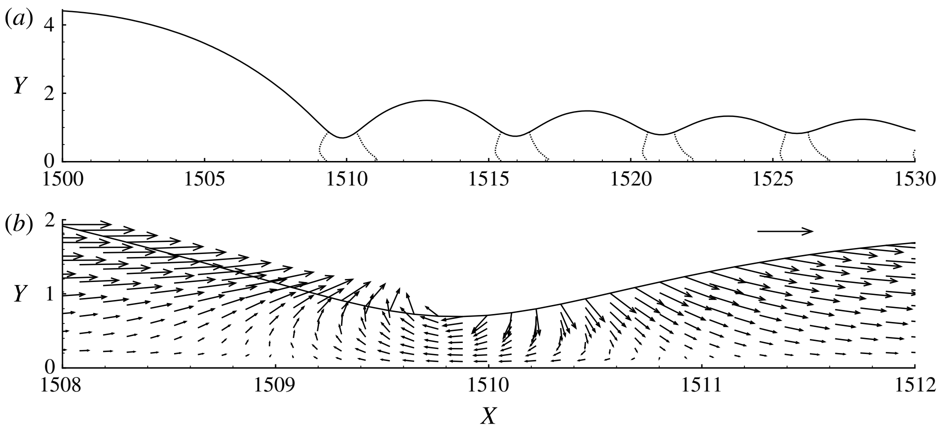

FIGURE 9. Flow reversal in the inertial regime at $\delta = 10$, for $\Gamma = 3400$ and a vertical wall. (*a*) Boundaries of flow reversal zones; (*b*) close-up view of the velocity field vectors in the laboratory frame.

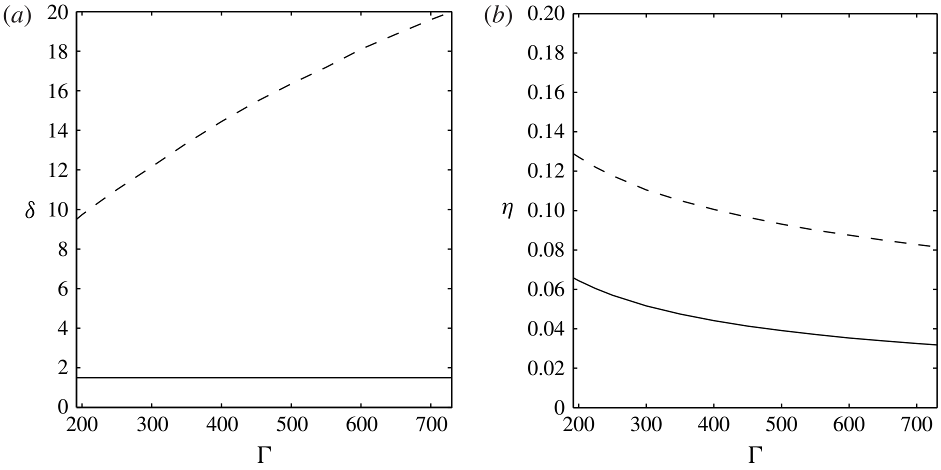

FIGURE 10. Parametric boundaries (lower: solid line, upper: dashed line) between which flow reversal occurs on a vertical wall. The same data are expressed as δ versus Γ in (*a*), and as η versus Γ in (*b*).

the streamwise velocity becomes in fact larger than the wave speed (in the case of figure 9, u reaches 2.878 as compared to $c = 2.565$).

The occurrence of backflow is systematically investigated in the DNS data by monitoring the minimum of the wall strain rate $\partial_y u|_{y=0}$. The results are parameterized in terms of δ and Γ (or equivalently in terms of η and Γ, as δ and η are related by $\eta = \delta^{4/11}\Gamma^{-6/11}$) and are shown in figure 10. The two curves, depicted in both subfigures, are respectively the lower and upper bound of the region of backflow. For example, figure 10(*a*) indicates that, for constant Γ, flow reversal is observed only above a minimum value of the reduced Reynolds number δ and below a maximum one.

The existence of a lower δ value below which backflow does not occur was documented experimentally by Tihon *et al.* (2006), who noticed that the solitary wave must reach a minimum height for flow reversal to be observed. However, the elimination of backflow above some upper δ value, despite the large height of the waves, is unexpected and appears to be reported here for the first time. A plausible explanation for the neglect of this upper limit is that it is an increasing function of $\varGamma$, and thus corresponds to very high waves in the commonly studies case of water ($\varGamma = 3400$). Indeed, the present computations could not provide reliable results above $\varGamma = 720$.

The aforementioned computational observations support further the idea that flow reversal has a capillary origin and is directly related to the amplitude of the capillary ripples. Indeed, the lower boundary $\delta \approx 1.5$ closely matches the sharp increase in the height of solitary waves that is observed in figure 3, and it is recalled that the amplitude of the capillary ripples and the height of the main hump are strongly correlated.

The occurrence of the upper limit is also in accord with this reasoning, because, as observed again from figure 3, at large δ the height of the main hump (and thus the amplitude of the capillary ripples) saturates. As a result, the capillary pressure gradient that promotes backflow also saturates, and is eventually overcome by the increasing inertia. This interplay between capillary and inertia forces, which leads to the elimination of capillary effects above a certain magnitude of inertia, is typical of many free-surface flows, see for example Bontozoglou & Serifi (2008). A crucial observation from figure 3 is that the saturation height is an increasing function of $\varGamma$. Thus, high-$\varGamma$ fluids exhibit capillary ripples of larger amplitude, and thus necessitate stronger inertia to eliminate the backflow phenomenon. This reasoning explains the dependence of the upper limit on $\varGamma$, as is depicted in figure 10(*a*).

An equivalent alternative explanation for the upper limit to backflow may be provided in terms of figure 10(*b*). For a given fluid, and thus a given value of $\varGamma$, raising the reduced Reynolds number δ is accompanied by an increase of the viscous dispersion parameter η. As η compares the viscous and capillary dampings of short waves, it follows that capillary ripples are more effectively attenuated by viscous effects at higher values of δ, which explains the onset of a second boundary above which flow reversal disappears. A viscous damping of the capillary ripples as the origin of the disappearance of flow reversal is supported by our numerical data. Indeed, the suppression of flow reversal is observed at a roughly constant value of η (see figure 10*b*).

5.4. *Effect of Froude number*

In this subsection we extend the previous results to the case of a wall with inclination less than 90°. In the frame of the scaling analysis of § 3, the extension will be done consistently in terms of the Froude number, because this is the key parameter for both the low-δ and the high-δ asymptotics (equations (3.9) and (3.20) respectively). The critical threshold of long-wave instability, $Re_c = (5/6)\cot\beta$, is written in terms of the Froude number as $Fr_c^{-2} = 2/5$. Thus, the range of Fr^{-2} that needs to be investigated is $[0, 0.4)$.

The parametric variation of c and h_m with Fr^{-2} for the case $\varGamma^* = 193$ is shown in figure 11. Here $\varGamma^*$ depends only on liquid properties and reverts to the previously used parameter, $\varGamma$, in the case of a vertical wall. It is observed that, for a constant δ, phase speed and wave height attain largest values for $Fr^{-2} = 0$ (vertical wall), and

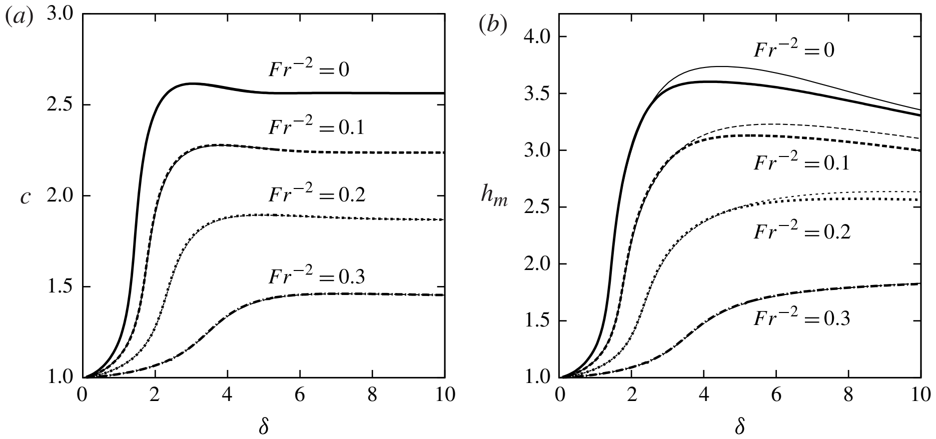

FIGURE 11. Phase speed (*a*) and height (*b*) of solitary waves as functions of δ for $\Gamma^*=193$ and different values of Fr^{-2}. Thick and thin lines refer respectively to DNS and to the four-equation model.

Fr^{-2}	$c_{\infty DNS}$ ($\pm 10^{-3}$)	$c_{\infty model}$ ($\pm 10^{-5}$)	Equation (3.20)
0	2.560	2.564 03	2.555 64
0.1	2.235	2.236 67	2.161 74
0.2	1.860	1.866 16	1.811 63
0.3	1.438	1.443 56	1.410 25

TABLE 2. Prediction of c_∞ for various *Fr* values by DNS, by the four-equation model and by the simplified equation (3.20).

decrease with the approach to the instability threshold $Fr^{-2}=0.4$. For this Γ^*, the agreement between DNS and the four-equation model remains excellent throughout the entire parameter range. The classification into drag–gravity and drag–inertia regimes is still valid, and the former regime expands to higher δ as Fr^{-2} decreases. Also, the maximum in the intermediate regime gradually declines, and eventually disappears at low-enough Fr^{-2}.

At the high-δ limit and for constant Fr^{-2}, the phase speed reaches a plateau, c_∞, as predicted by asymptotic theory equation (3.20). The simplified prediction of (3.20) is compared in table 2 to the result of DNS and to the rigorous prediction of the four-equation model (the last two obtained by the procedure outlined in (5.1)).

The above results refer to a single $\Gamma^*=193$. For completeness, we compare in figure 12 data for $\Gamma^*=193$ and $\Gamma^*=3400$, keeping $\delta=10$ constant and spanning the entire range of Fr^{-2}. Figure 12(*a*) plots DNS data for c, and shows that it is insensitive to Γ^*, and that it varies roughly linearly with $Fr^{-2}-Fr_c^{-2}$. Figure 12(*b*) plots DNS data for h_m, and shows that the variation with Γ^* (which expresses the effect of viscous dispersion, as exhibited for example by figure 3*b*) diminishes with the approach to Fr_c^{-2}. Finally, figure 12(*c*) compares the previous DNS data on c and h_m with predictions of the four-equation model.

Though the aforementioned description in terms of Fr^{-2} is convenient for comparisons with asymptotic theory, it might be confusing from the point of view

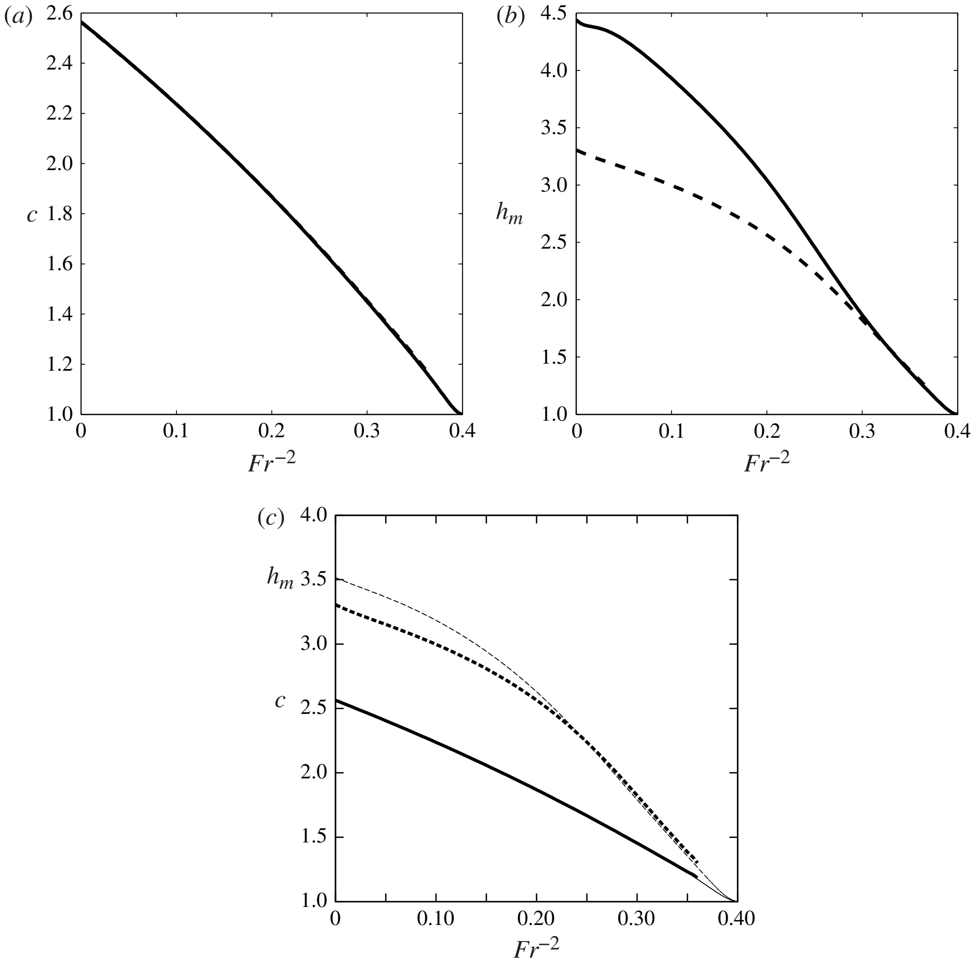

FIGURE 12. (*a*) Phase speed and (*b*) height of solitary waves as functions of Fr^{-2}, obtained by DNS at $\delta = 10$. Solid and dashed lines refer respectively to $\varGamma^* = 3400$ and $\varGamma^* = 193$. (*c*) Comparison of the DNS results in (*a,b*) for $\varGamma^* = 193$ (thick lines) to predictions of the four-equation model (thin lines).

of a physical experiment. Thus, we note that, in figure 11, only the curve $Fr^{-2} = 0$ corresponds to constant inclination ($\beta = 90°$). Moving along a constant $Fr^{-2} \neq 0$ curve in the direction of decreasing δ amounts to a simultaneous decrease of $\cot\beta$ and *Re*, so that at the origin the values $\beta = 90°$ and $Re = 0$ are reached. Equivalently, the variation of the properties of solitary waves along an inclined wall with a specific $\beta \neq 90°$ will be described by a curve that starts tangential to the *x*-axis ($c = 1$, $Re = Re_c$) at the respective critical δ value,

$$\delta_c = (2.5 \cot\beta)^{11/9}\, \varGamma^{-1/3} = (2.5 \cot\beta)^{11/9}\, (\sin\beta)^{1/9}\, (\varGamma^*)^{-1/3}\,, \tag{5.2}$$

rises with increasing *Re* crossing the $Fr^{-2} = \text{const}$ curves and eventually approaches $Fr^{-2} = 0$ asymptotically from below at high *Re*.

6. Conclusions

Models of reduced dimensionality, based on long-wave expansions, are an indispensable tool in the analysis of liquid film flow. However confidence in their use is severely undercut by the large differences they exhibit in the drag–inertia regime, i.e. when the reduced Reynolds number δ becomes large. Not only do they predict widely different values for the height and phase speed of stationary solitary waves, but they also vary qualitatively in the parametric dependence of these properties on δ.

Motivated by the desire to resolve this issue, the present work reports systematic numerical simulations of stationary solitary waves under a wide range of conditions. First, the case of a vertical wall is considered in detail. Based on the DNS results, it is concluded that the balance of inertia and capillarity, which dominates the properties of solitary waves in the drag–inertia regime, is highly non-trivial (recall that in the drag–gravity regime, close enough to the instability threshold, inertia and capillarity provide merely perturbations around the main balance of viscous and gravity forces). More specifically, the curves describing the variation of wave height and phase speed with δ are found to have an unexpectedly complex shape, with multiple inflection points and maxima at intermediate values. All one- and two-equation models fail to predict this behaviour, as they exhibit monotonic variation with δ.

On the contrary, the four-equation model by Ruyer-Quil & Manneville (2000) predicts correctly all the qualitative trends, and is in satisfactory quantitative agreement with the data up to a Kapitza number of the order $\Gamma \approx 5000$. One value of particular significance is the phase velocity, c_∞, in the limit of high δ, which is independent of Γ and may be predicted by asymptotic analysis of the back tail of the wave where the effect of surface tension is negligible. Again the various one- and two-equation models provide different results in the range $c_\infty = 1.5$–3.0, whereas the four-equation model predicts $c_\infty = 2.564$, in close agreement with the DNS value $c_\infty = 2.560$. Thus, we mainly concentrated on the four-equation model, and set its predictions in detailed perspective with the DNS data.

A demanding test is the calculation of the detailed shape of the solitary-wave tails. This is expressed by the eigenvalues of the linearized equations of motion, of which one is real and corresponds to the monotonic rise of the upstream tail, and the other two are complex conjugate and describe the oscillatory decline of the downstream tail. The former is well predicted by the model over the entire range of δ, but the latter shows large deviations at high δ. As a consequence, the model does not capture correctly the number and decline rate of front-running capillary ripples deep in the drag–inertia regime. It is suspected that this failure constitutes an inherent limitation of the boundary-layer equations, which represent the first step towards all the models of reduced dimensionality. However, this conjecture remains to be rigorously proven.

Interesting information is derived from the DNS data about the local flow reversal in front of the main hump, which has been extensively discussed in the recent literature. More specifically, it is found that flow reversal occurs for a limited range of δ, appearing only beyond $\delta \approx 1.5$, and disappearing above a higher δ that is an increasing function of Γ. These results are interpreted in terms of the amplitude of capillary ripples, and confirm conclusively that capillary pressure is the driving mechanism for the phenomenon.

Finally, the previous results are extended to cover the entire range of Froude numbers $(0, 0.4)$, providing benchmark data for non-vertical wall inclinations. All the parameters are shown to decrease as the critical condition $Fr^{-2} = 0.4$ is approached, and thus it is confirmed that the case of a vertical wall ($Fr^{-2} = 0$), which has been considered in detail, represents the most demanding test of the models. Based on their performance assessed here in comparison to DNS data, it is concluded that the most successful among them, i.e. the four-equation model, is accurate enough to be used for the analysis of problems of heat/mass transfer in future research.

Another research topic that is motivated by the present work, is the study of non-stationary dynamics. Judging from the complexity of stationary solitary waves in the drag–inertia regime that is revealed by the present numerical results, it may be conjectured that the non-stationary dynamics of interacting waves will be highly non-trivial and even more interesting. The recent study of Pradas *et al.* (2013) provides strong evidence in support of this view.

Acknowledgement

The present work was supported by the EU under the Marie-Curie Initial Training Network 'Multiflow' (GA no:214919-2).

REFERENCES

ALEKSEENKO, S. V., NAKORYAKOV, V. Y. & POKUSAEV, B. G. 1985 Wave formation on a vertical falling liquid film. *AIChE J.* **31**, 1446–1460.

BACH, P. & VILLADSEN, J. 1984 Simulation of the vertical flow of a thin wavy film using a finite element method. *Intl J. Heat Mass Transfer* **27**, 815–827.

BALMFORTH, N. J. & LIU, J. J. 2004 Roll waves in mud. *J. Fluid Mech.* **519**, 33–54.

BENNEY, D. J. 1966 Long waves on liquid films. *J. Math. Phys.* **45**, 150–155.

BONTOZOGLOU, V. & SERIFI, K. 2008 Falling film flow along steep two-dimensional topography: the effect of inertia. *Intl J. Multiphase Flow* **34**, 734–747.

BREVDO, L., LAURE, P., DIAS, F. & BRIDGES, T. J. 1999 Linear pulse structure and signalling in a film flow on an inclined plane. *J. Fluid Mech.* **396**, 37–71.

BUNOV, A., DEMEKHIN, E. & SHKADOV, V. Y. 1986 Bifurcations of solitary waves in a flowing liquid film. *Vestnik Moskov. Univ. Ser. I Mat. Mekh.* **41** (2), 37–38.

CHANG, H.-C. & DEMEKHIN, E. A. 2002 In *Complex Wave Dynamics on Thin Films* (ed. D. Möbius & R. Miller), Elsevier.

CRASTER, R. V. & MATAR, O. K. 2009 Dynamics and stability of thin liquid films. *Rev. Mod. Phys.* **81**, 1131–1198.

DIETZE, G. F., AL-SIBAI, F. & KNEER, R. 2009 Experimental study of flow separation in laminar falling liquid films. *J. Fluid Mech.* **637**, 73–104.

DIETZE, G. F., LEEFKEN, A. & KNEER, R. 2008 Investigation of the backflow phenomenon in falling liquid films. *J. Fluid Mech.* **595**, 435–459.

DOEDEL, E. J., CHAMPNEYS, A. R., FAIRGRIEVE, T. F., KUZNETSOV, Y. A., SANDSTEDE, B. & WANG, X.-J. 2007 Auto07: Continuation and bifurcation software for ordinary differential equations. *Tech. Rep.* Department of Computer Science, Concordia University, Montreal, Canada (available by FTP from ftp.cs.concordia.ca in directory pub/doedel/auto).

GAO, D., MORLEY, N. B. & DHIR, V. 2003 Numerical simulation of wavy falling film flow using VOF method. *J. Comput. Phys.* **192**, 624–642.

GJEVIK, B. 1970 Occurrence of finite-amplitude surface waves on falling liquid films. *Phys. Fluids* **13**, 1918–1925.

HO, L.-W. & PATERA, A. T. 1990 A legendre spectral element method for simulation of unsteady incompressible viscous free-surface flows. *Comput. Meth. Appli. Mech. Engng* **80**, 355–366.

HOFFMANN, K. A. & CHIANG, S. T. 2000 *Computational Fluid Dynamics*. EES.

HOOD, P. 1976 Frontal solution program for unsymmetric matrices. *Intl J. Numer. Meth. Engng* **10**, 379–399.

JAYANTI, S. & HEWITT, G. F. 1996 Hydrodynamics and heat transfer of wavy thin film flow. *Intl J. Heat Mass Transfer* **40**, 179–190.

KALLIADASIS, S., RUYER-QUIL, C., SCHEID, B. & VELARDE, M. G. 2012 *Falling Liquid Films*. Springer.

KAPITZA, P. L. & KAPITZA, S. P. 1949 Wave flow of thin layers of a viscous fluid: III. experimental study of undulatory flow conditions. In *Collected papers of P. L. Kapitza (1965)* (ed. D. T. Haar), pp. 690–709. Pergamon, (Original paper in Russian: *Zh. Ekper. Teor. Fiz.* **19, 105–120**).

KARAPANTSIOS, T. D., PARAS, S. V. & KARABELAS, A. J. 1989 Statistical characteristics of free falling films at high Reynolds numbers. *Intl J. Multiphase Flow* **15**, 1–21.

KUNUGI, T. & KINO, C. 2005 DNS of falling film structure and heat transfer via MARS method. *Comput. Struct.* **83**, 455–462.

LEONTIDIS, V., VATTEVILLE, J., VLACHOGIANNIS, M., ANDRITSOS, N. & BONTOZOGLOU, V. 2010 Nominally two-dimensional waves in inclined film flow in channels of finite width. *Phys. Fluids* **22**, 112106.

LIU, J. & GOLLUB, J. P. 1994 Solitary wave dynamics of film flows. *Phys. Fluids* **6**, 1702–1712.

LIU, Q. Q., CHEN, L., LI, J. C. & SINGH, V. P. 2005 Roll waves in overland flow. *J. Hydrol. Engng* **10** (2), 110–117.

MALAMATARIS, N., VLACHOGIANNIS, M. & BONTOZOGLOU, V. 2002 Solitary waves on inclined films: flow structure and binary interactions. *Phys. Fluids* **14**, 1082–1094.

MIYARA, A. 2000*a* Numerical analysis for a falling liquid film with interfacial waves on an inclined plate. part 2: Effects of interfacial waves on flow dynamics and heat transfer. *Heat Transfer Asian Res.* **29** (3), 233–248.

MIYARA, A. 2000*b* Numerical simulation of wavy liquid film flowing down on a vertical wall and an inclined wall. *Intl J. Therm. Sci.* **39** (9), 1015–1027.

NGUYEN, L. T. & BALAKOTAIAH, V. 2000 Modeling and experimental studies of wave evolution on free falling viscous films. *Phys. Fluids* **12**, 2236–2256.

NOSOKO, T. & MIYARA, A. 2004 The evolution and subsequent dynamics of waves on a vertically falling liquid film. *Phys. Fluids* **16**, 1118–1126.

OOSHIDA, T. 1999 Surface equation of falling film flows with moderate Reynolds number and large but finite Weber number. *Phys. Fluids* **11**, 3247–3269.

ORON, A., GOTTLIEB, O. & NOVBARI, E. 2009 Numerical analysis of a weighted-residual integral boundary-layer model for nonlinear dynamics of falling liquid films. *Eur. J. Mech. B/Fluids* **28**, 1–36.

PANGA, M. K. R. & BALAKOTAIAH, V. 2003 Low-dimensional models for vertically falling viscous films. *Phys. Rev. Lett.* **90** (15), 154501.

PRADAS, M., KALLIADASIS, S., NGUYEN, P.-K. & BONTOZOGLOU, V. 2013 Bound-state formation in interfacial turbulence: direct numerical simulations and theory. *J. Fluid Mech.* **716** (R2).

PUMIR, A., MANNEVILLE, P. & POMEAU, Y. 1983 On solitary waves running down an inclined plane. *J. Fluid Mech.* **135**, 27–50.

RAMASWAMY, B., CHIPPADA, S. & JOO, S. W. 1996 A full-scale numerical study of interfacial instabilities in thin-film flows. *J. Fluid Mech.* **325**, 163–194.

ROBERTS, A. J. 1996 Low-dimensional models of thin film fluid dynamics. *Phys. Lett.* A **212**, 63–71.

ROBERTS, A. J. & LI, Z.-Q. 2006 An accurate and comprehensive model of thin fluid flows with inertia on curved substrates. *J. Fluid Mech.* **553**, 33–73.

RUYER-QUIL, C. & KALLIADASIS, S. 2012 Wavy regimes of film flow down a fibre. *Phys. Rev.* E **85**, 046302.

RUYER-QUIL, C. & MANNEVILLE, P. 1998 Modeling film flows down inclined planes. *Eur. Phys. J.* B **6**, 277–292.

RUYER-QUIL, C. & MANNEVILLE, P. 2000 Improved modelling of flows down inclined planes. *Eur. Phys. J.* B **15**, 357–369.

RUYER-QUIL, C. & MANNEVILLE, P. 2002 Further accuracy and convergence results on the modelling of flows down inclined planes by weighted-residual approximations. *Phys. Fluids* **14**, 170–183.

RUYER-QUIL, C. & MANNEVILLE, P. 2005 On the speed of solitary waves running down a vertical wall. *J. Fluid Mech.* **531**, 181–190.

RUYER-QUIL, C., TREVELEYAN, P., GIORGIUTTI-DAUPHINÉ, F., DUPRAT, C. & KALLIADASIS, S. 2008 Modelling film flows down a fibre. *J. Fluid Mech.* **603**, 431–462.

SALAMON, T. R., ARMSTRONG, R. C. & BROWN, R. A. 1994 Traveling waves on vertical films: numerical analysis using the finite element method. *Phys. Fluids* **6**, 2202–2220.

SAMANTA, A., GOYEAU, B. & RUYER-QUIL, C. 2013 A falling film on a porous medium. *J. Fluid Mech.* **716**, 414–444.

SAMANTA, A., RUYER-QUIL, C. & GOYEAU, B. 2011 A falling film down a slippery inclined plane. *J. Fluid Mech.* **684**, 353–383.

SCHEID, B., RUYER-QUIL, C. & MANNEVILLE, P. 2006 Wave patterns in film flows: modelling and three-dimensional waves. *J. Fluid Mech.* **562**, 183–222.

SCHEID, B., RUYER-QUIL, C., THIELE, U., KABOV, O. A., LEGROS, J. C. & COLINET, P. 2005 Validity domain of the Benney equation including the Marangoni effect for closed and open flows. *J. Fluid Mech.* **527**, 303–335.

SHKADOV, V. YA. 1967 Wave flow regimes of a thin layer of viscous fluid subject to gravity. *Izv. Ak. Nauk SSSR, Mekh. Zhidk Gaza* **1**, 43–51; English translation in *Fluid* Dyn. **2**, 29–34, 1970 (Faraday Press, NY).

SHKADOV, V. YA. 1977 Solitary waves in a layer of viscous liquid. *Izv. Ak. Nauk SSSR, Mekh. Zhidk Gaza* **1**, 63–66.

THOMAS, H. A. 1939 The propagation of waves in steep prismatic conduits In *Proc. Hydraulics Conf., Univ. of Iowa*, pp. 214–229.

TIHON, J., SERIFI, K., ARGYIRIADI, K. & BONTOZOGLOU, V. 2006 Solitary waves on inclined films: their characteristics and the effects on wall shear stress. *Exp. Fluids* **41**, 79–89.

TRIFONOV, Y. Y. 2012 Stability and bifurcations of the wavy film flow down a vertical plate: the results of integral approaches and full-scale computations. *Fluid Dyn. Res.* **44**, 031418.

WHITHAM, G. B. 1974 *Linear and Nonlinear Waves*. John Wiley & Sons.

YU, L.-Q., WASDEN, F. K., DUKLER, A. E. & BALAKOTAIAH, V. 1995 Nonlinear evolution of waves on falling films at high Reynolds numbers. *Phys. Fluids* **7**, 1886–1902.